Corrosion Behavior, Microstructure and Mechanical Properties of Novel Mg-Zn-Ca-Er Alloy for Bio-Medical Applications

Devadas Bhat Panemangalore, Rajashekhara Shabadi, Manoj Gupta

metals

MDPI

Article

Corrosion Behavior, Microstructure and Mechanical Properties of Novel Mg-Zn-Ca-Er Alloy for Bio-Medical Applications

Devadas Bhat Panemangalore [1], Rajashekhara Shabadi [2,3,4,5,*] and Manoj Gupta [6]

1 Department of Metallurgical and Materials Engineering, National Institute of Technology Karnataka, Surathkal 575025, India; devadasbhatp@nitk.edu.in
2 UMR 8207-UMET-Unité Matériaux et Transformations, University Lille, F-59000 Lille, France
3 CNRS, UMR 8207 UMET, F-59000 Lille, France
4 INRAE, F-59000 Lille, France
5 Centrale Lille, F-59000 Lille, France
6 Department of Mechanical Engineering, National University of Singapore, 9 Engineering Drive 1, Singapore 117576, Singapore; mpegm@nus.edu.sg
* Correspondence: rajashekhara.shabadi@univ-lille.fr; Tel.: +33-(0)-320-33-62-24; Fax: +33-(0)-320-43-65-91

Abstract: In this study, the effect of calcium (Ca) and erbium (Er) on the microstructure, mechanical properties, and corrosion behavior of magnesium-zinc alloys is reported. The alloys were prepared using disintegrated melt deposition (DMD) technique using the alloying additions as Zn, Ca, and Mg-Er master alloys and followed by hot extrusion. Results show that alloying addition of Er has significantly reduced the grain sizes of Mg-Zn alloys and also when compared to pure magnesium base material. It also has substantially enhanced both the tensile and the compressive properties by favoring the formation of $MgZn_2$ type secondary phases that are uniformly distributed during hot-extrusion. The quaternary Mg-Zn-Ca-Er alloy exhibited the highest strength due to lower grain size and particle strengthening due to the influence of the rare earth addition Er. The observed elongation was a result of extensive twinning observed in the alloys. Also, the degradation rates have been substantially reduced as a result of alloying additions and it is attributed to the barrier effect caused by the secondary phases.

Keywords: magnesium; disintegrated melt deposition; microstructure; corrosion

Citation: Panemangalore, D.B.; Shabadi, R.; Gupta, M. Corrosion Behavior, Microstructure and Mechanical Properties of Novel Mg-Zn-Ca-Er Alloy for Bio-Medical Applications. *Metals* **2021**, *11*, 519. https://doi.org/10.3390/met11030519

Academic Editor: Dmytro Orlov

Received: 3 February 2021
Accepted: 19 March 2021
Published: 22 March 2021

1. Introduction

In the field of medicine, since the beginning of the last century, there has been tremendous research ongoing using magnesium as orthopedic and cardiovascular bio-implants. This is because of its attractive density and elastic modulus that are akin to the natural bone. Apart from its similar physical and mechanical properties, its degradability after it has fulfilled its purpose improvises over conventional implants made of titanium and stainless steel that require a second surgery to remove from the body [1]. Hence, magnesium is not only biocompatible but also biodegradable in bodily fluids and the degraded magnesium furnishes as a dietary requirement. However, the challenge here is to have the bio-degradation of the implant in a controlled manner. Otherwise, there is a risk of toxicity by excessive release of ions. This concern also addresses the release of erbium.

Being placed high on the periodic table, pure magnesium is electrochemically active and corrosive in conducive environments [2]. Alloying additions can improve their physical, mechanical, and corrosion behavior and that is determined by the quantity, distribution, and processing methodologies. Among several alloying additions, commercially produced magnesium alloys include manganese (Mn), aluminum (Al), zinc (Zn), zirconium (Zr), and rare earth (RE). For engineering applications, these alloying additions are tailored only to minimize the cost of the final product and maximize the mechanical properties. In contrast, for biomedical applications, addition of elements must be considered carefully as

they should not be harmful in-vivo. Several commercial alloys like AZ31 [3] and AZ91 [4] which have excellent mechanical properties and corrosion resistance have been tried as an implant material unsuccessfully. This is because the addition of aluminum contents in the bio-implants may induce neurotoxicity that might contribute to Alzheimer's disease and hence it is not beneficial as an alloying element [5]. Hence, there is a need for careful selection of alloying elements that could respond to the controlled bio-degradability without being harmful to the human body.

Zinc as an alloying element for magnesium is only second best to aluminum in terms of its effectiveness that helps in the enhancement of ductility and deformability of magnesium. It increases strength via age hardening and solid solution strengthening effect [6]. It enhances the corrosion resistance by elevating the corrosion potential of magnesium alloy [7]. For the human body, Zn is very essential for the immune system. It acts as a co-factor for specific enzymes in bones and cartilage. Tensile and tensile-creep properties of blend and hot-pressed Mg-*x*Zn (x = 2.9, 3.3, 4, and 4.4 wt.%) were studied by Boehlert et al. [8]. Peng et al. studied the effects of backward extrusion on the mechanical and degradation behavior of Mg-*x*Zn (x-0.5, 1, 1.5, and 2 wt.%) in the simulated-body-fluid (SBF) solution [9]. Bakhsheshi-Rad et al. [10] studied the bio-corrosion behavior of Mg-*x*Zn (x = 1.25, 2.5, and 4 wt.%) and defined a relationship between solidification behavior and corrosion rate. Mg-2.5Zn was synthesized by Parande et al. [11] using a blend-press-sinter powder metallurgy technique. For sintering, they used a hybrid microwave setup, and then these compacts were extruded. The alloy exhibited not only excellent mechanical properties but good damping characteristics too.

In bones, calcium forms a major component. The recommended daily allowance (RDA) of calcium by the doctors is 1000 mg for adults [12]. The density of Ca is 1.55 g/cm^3, which is similar to that of low density Mg. Also, in terms of metallurgical properties, this is an excellent grain refiner and it can reduce the effect of oxidation during solidification conditions [13,14]. With a low weight percentage addition, it can enhance the mechanical properties and corrosion resistance [15]. In the binary Mg-Ca system, the phase Mg_2Ca improves creep resistance due to all three strengthening mechanisms (solid-solution strengthening, precipitation strengthening, and grain boundary pinning). Hot-tearing and sticking are some of the problems occurring when large amounts of calcium are introduced. The addition of calcium is essential to inhibit oxidation during the solidification process as it forms a thin and dense CaO film [16]. Mg-Ca is also a good age-hardening system [17]. Several studies mention about a Mg-Ca binary system: Li et al. [18] fabricated binary Mg-*x*Ca (x = 1, 2, and 3 wt.%) alloys. The mechanical properties were enhanced for as-rolled condition as compared to as-cast and were further enhanced for as-extruded alloys. This is due to thermomechanical processing leading to the refinement of grain sizes. Drynda et al. [12] studied alloying of low calcium amounts (up to 4 wt.%) that led to increment in ultimate tensile strength up to 210–240 MPa. The grain size values did not change for various increments in calcium content. Precipitation hardening behavior of Mg-Ca alloys was studied by Nie et al. and Mg-1Ca alloy exhibits a moderate precipitation-hardening response during isothermal aging at 200 °C [17].

Erbium is relatively new as an alloying element to magnesium. This was used before as mischmetal along with other rare-earths but its effects have not been discussed in detail in the literature. Rare earth toxicology evaluation was conducted by Rim et al. and they categorized erbium to be of low to moderate toxicity [19]. Leng et al. studied biocorrosion of Mg-8Y-1Er-2Zn in SBF [20]. Zhang et al. studied Mg-8Er-1Zn alloy for its biomedical applications [7]. The amount of RE addition in the abovementioned alloys targeting biomedical applications was significantly high. RE element erbium can significantly enhance the corrosion resistance of Mg alloys [21]. Hao et al. investigated a quaternary Mg-8Er-5Sn-0.5Zr with a rather high addition of erbium [22]. The extruded and annealed alloy exhibited superior mechanical properties (Yield stress = 310 MPa and elongation 14%) and the microstructure comprised of α-Mg, block W phase, and high-density fine lamellar-shaped long period stacking order (LPSO) phase. The effect of the Zn/Er weight ratio on

phase formation and mechanical properties of as-cast Mg-Zn-Er was studied by Li et al. [23]. They have seen that when this ratio is less than 0.8, W-phase with a face-centered cubic structure is obtained. Above the ratio of 6 until 10, the formation of I-phase with an icosahedral quasicrystalline structure is feasible. When the ratio is in the range of 1 and 4, these two phases co-exist. To investigate the effect of heat-treatment on the microstructure evolution and the mechanical properties of Mg-Zn-Er system, Zhao et.al synthesized Mg-Zn-0.63Er containing icosahedral quasicrystalline phase (I-phase) [24]. Rod-like $MgZn_2$ particles formed during synthesis were responsible for enhanced tensile strength.

In this study, the microstructure and mechanical behavior of biocompatible Ca and Er alloyed Mg-2Zn extruded materials are discussed, in comparison to pure Mg. A low amount of expensive erbium is added to achieve better properties with minimal toxicity. The tensile behavior of the quaternary alloy is reported in detail by correlating to the material's microstructure. The degradation rates in both NaCl and phosphate buffer saline (PBS) medium are discussed.

2. Materials and Methods

2.1. Processing

Mg-2wt.%Zn-0.6wt.%Ca-1wt.%Er was synthesized by melting commercially pure Mg turnings (Acros Organics, Geel, Belgium; 99.9% purity), zinc pellets (Alfa Aesar, Karlsruhe, Germany; 99.9% purity), calcium pellets (Alfa Aesar, Karlsruhe, Germany; 99.9% purity) and Mg-30wt.%Er master alloy (Sunrelier Metal Co, Limited, Shanghai, China) using the disintegrated melt deposition (DMD) method [25]. Upon reaching the superheat temperature of 840 °C in an argon atmosphere, the melt was stirred for 5 min at approximately 450 rpm and it is bottom-poured. During pouring, the molten slurry was disintegrated by two jets of argon gas at 90° and the melt was deposited into a stainless-steel mold. After heat treatment at 400 °C for 1h, the machined ingots of 36 mm diameter are hot-extruded using an extrusion ratio of 20.25:1 at 350 °C to produce rods of 8 mm diameter.

2.2. Microstructural Characterization

To study texture and identify the presence of secondary phases, X-ray diffraction studies along the longitudinal sections of extruded rods were carried out. The X-ray diffraction characterization of the samples was carried out using a Rigaku SMART LAB multipurpose diffractometer (Rigaku Corporation, Tokyo, Japan). The operating conditions used were 9 kW rotating anode, operated at 45 kV and 200 mA in Parallel Beam mode. It consisted of a PSD 1D detector DTEX, delivering Cu-Kα radiation (λ = 1.5418 Å). The $2\theta/\Omega$ scans were performed between 20° and 100° with a scan speed of 3°/min and a 0.01° step size.

Samples for microstructural characterization were as per the metallography standards. They were later polished using Fischione SEM-Ion mill to remove fine scratches and strain gradients on the surface for Electron Back Scattered Diffraction (EBSD, Oxford Instruments, Oxfordshire, UK) analysis. ZEISS Optical microscope and JEOL Scanning Electron Microscope (SEM) coupled with Energy Dispersive Spectroscopy (EDS) (JEOL, Tokyo, Japan) were used for the microstructural studies. To perform quantitative microstructural analysis and to identify the orientation (texture) of the alloys, Electron Back Scattered Diffraction (EBSD) was used. The SEM coupled with Oxford Instruments EDS/EBSD coupled system (80 mm^2 SDD spectrometer and HKl Nordlys Max2 EBSD camera, Oxford Instruments, Oxfordshire, UK).

2.3. Mechanical Properties

2.3.1. Microhardness

Microhardness measurements were carried out on the as-extruded samples using BUEHLER digital Microhardness tester (Illinois Tool Works, Glenview, IL, USA). Vickers indenter under a test load of 500 gf and a dwell time of 15 s was used to perform

the microhardness tests following the ASTM: E384-11e1. The tests were conducted for 15 repeatable readings.

2.3.2. Tensile Test

A fully automated servo-hydraulic mechanical testing machine, Model-MTS 810 (MTS, Saint Paul, MN, USA) was used to determine the tensile properties of the developed materials, following ASTM: E8/8M-13a. The crosshead speed was set at 0.254 mm/min. Specimens with 5 mm diameter and 25 mm gauge length were used. Instron 2630-100 series clip-on type extensometer (Instron, Singapore) was used to measure the elongation to failure. For each composition, a minimum of 5 tests were conducted to obtain repeatable values. The fracture surface analyses of materials tested under tension were studied using JEOL JSM-7800F LV SEM (JEOL, Tokyo, Japan).

2.3.3. Damping Characteristics

The impulse excitation technique (IMCE, Genk, Belgium) was used to measure the elastic modulus of the samples. A pre-defined shape of the extruded rod sample (60 mm length and 7 mm diameter) was taken and it was gently tapped to measure the resonant frequency that is unique for a given material. Using dimensions, mass, and resonant frequency, the elastic properties of the material were calculated.

2.4. Corrosion Behavior

To evaluate the corrosion behavior, immersion test and H_2 evolution studies were carried out in 0.5 wt.% NaCl medium at 25 °C and PBS solution at 37 °C to study the general corrosion and bio-corrosion behavior respectively. The samples before and after immersion were weighed. After immersion, they were cleaned with chromic acid (ASTM G1-90) to remove corrosion products. The equation used to determine the corrosion rate (CR) for immersion test measurements is:

$$CR = 2.1 * \Delta W$$

where ΔW is the weight loss rate (mg cm^{-2} day^{-1})

For the H_2 evolution test, each sample immersed in the corrosive environment was covered with an inverted flask and a graduated cylinder was used to collect H_2 bubbles. The volume of H_2 released was measured and the equation used to determine the corrosion rate for H_2 evolution is:

$$CR = 2.279 * V_H$$

where V_H is the hydrogen evolution rate (mL $cm^{-2}day^{-1}$)

3. Results

3.1. Microstructural Characterization

3.1.1. X-ray Diffraction

The effects of zinc, calcium, and erbium on the crystallographic orientation of pure Mg are analyzed using the X-ray diffraction (XRD) studies. Figure 1 shows the X-ray diffraction results of Mg-2Zn-0.6Ca-1Er obtained from the longitudinal sections of the samples. The X-ray diffraction results of pure Mg are presented for reference purposes. In the X-ray diffraction analysis of as extruded pure magnesium, the peaks observed at 2θ = 32°, 34°, 36° correspond to (1 0 $\bar{1}$ 0) prismatic, (0 0 0 2) basal and (1 0 $\bar{1}$ 1) pyramidal planes of hcp Mg-crystal. For pure Mg and Mg-2Zn-0.6Ca-1Er, the peaks are identified and they correspond to the diffraction planes of pure Mg. The secondary phase $MgZn_2$ is detected for Mg-2Zn-0.6Ca-1Er.

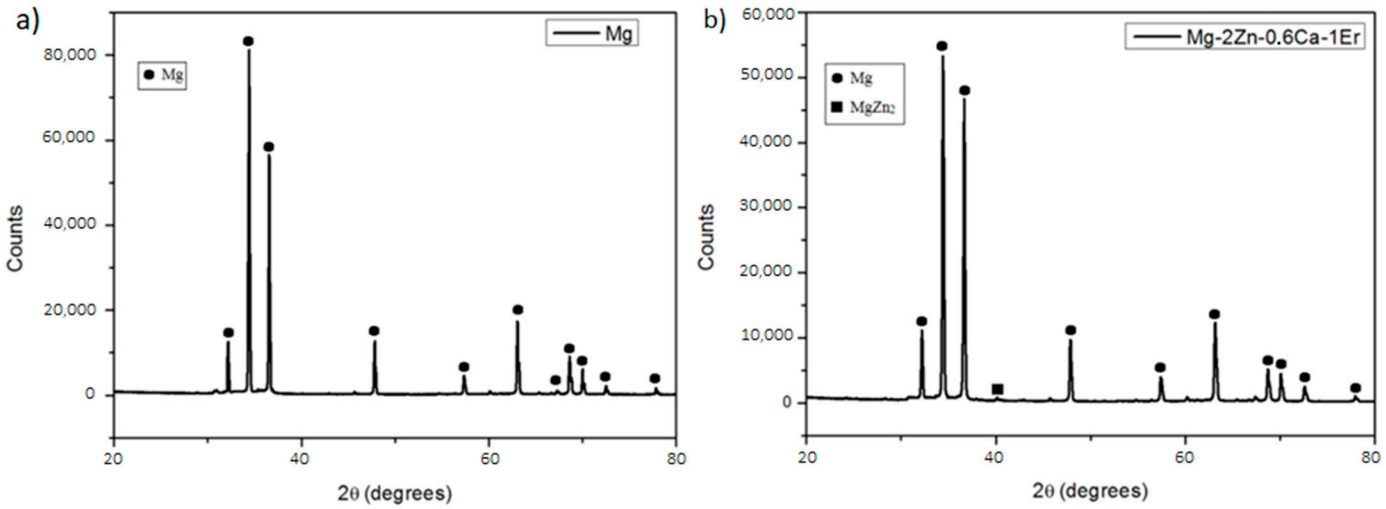

Figure 1. (**b**) X-ray diffraction results of extruded Mg-2Zn-0.6Ca-1Er in the longitudinal direction. (**a**) The XRD plot for pure Mg is presented for reference.

3.1.2. Optical Microscopy

Figure 2 illustrates the optical microstructure of Mg-2Zn-0.6Ca-1Er in the direction parallel to extrusion. Extrusion has helped the complete elimination of porosity that was evident after the disintegrate melt deposition. A recrystallized, near equiaxed grain structure, is observed after the extrusion process. The alloy exhibits slightly fine microstructure and it constitutes the matrix α phase and a small volume of second phases with different morphologies that are aligned along the extrusion direction and mostly on the grain boundaries. The secondary phases morphologies are of different shapes, including small-sized irregular particles and some rod-like which are elongated in the extrusion direction. These particles could have been broken down from the bigger size particles as evidenced elsewhere [21].

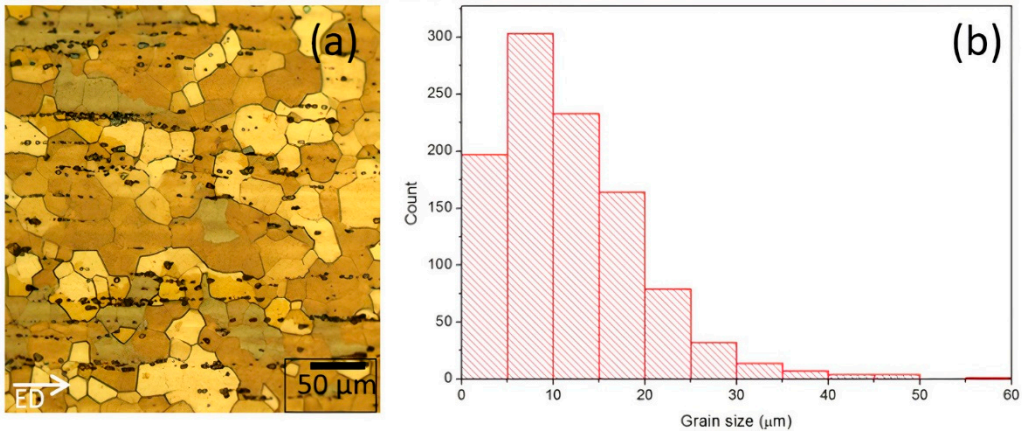

Figure 2. (**a**) Optical microstructure and (**b**) grain size histogram of Mg-2Zn-0.6Ca-1Er.

The average grain size was calculated in the EBSD images using ImageJ software. The grain size histogram is plotted in Figure 2. Pure Mg exhibited a grain size of 22.42 ± 0.7 µm [26] and that was reported in our earlier work. The combined influence of the alloying elements (zinc, calcium, and erbium) has substantially reduced the grain size and the mean value calculated is 11.57 ± 0.5 µm.

3.1.3. Scanning Electron Microscopy

Elemental mapping was carried out using EDS to study the distribution of zinc, calcium, and erbium in the as-DMDed and as-extruded alloy. The analysis for as-DMDed

and as-extruded alloys is shown in Figures 3 and 4 respectively. The back-scattered electron (BSE) image for as-DMDed alloy shows large grains and coarse secondary phases. These secondary phases are present in a network that exhibits several morphologies. Typical random morphologies were exhibited by the secondary phases of as-DMDed alloys. As-extruded alloys show α-Mg grains with white-island like second phases aligned along the extrusion direction. These second phases have been broken down after hot-extrusion into finely shaped phases. In both as-DMDed and as-extruded alloys, no segregation of elements could be seen. The EDS analysis for the phases for as-DMDed and as-extruded samples did not show a lot of difference and the elemental distribution was seen throughout the analyzed portion of the sample.

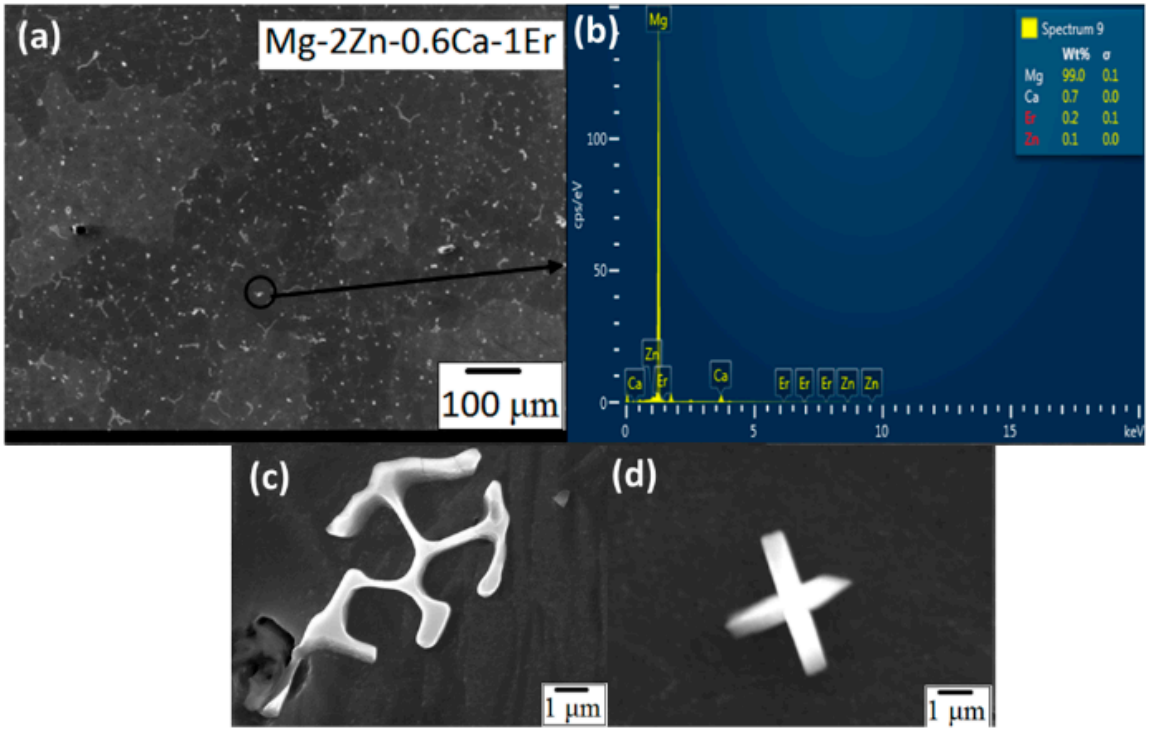

Figure 3. (**a**) SEM image, (**b**) EDS-analysis, (**c**,**d**) intermetallic phase constituents of as- disintegrated melt deposited (DMDed) Mg-2Zn-0.6Ca-1Er.

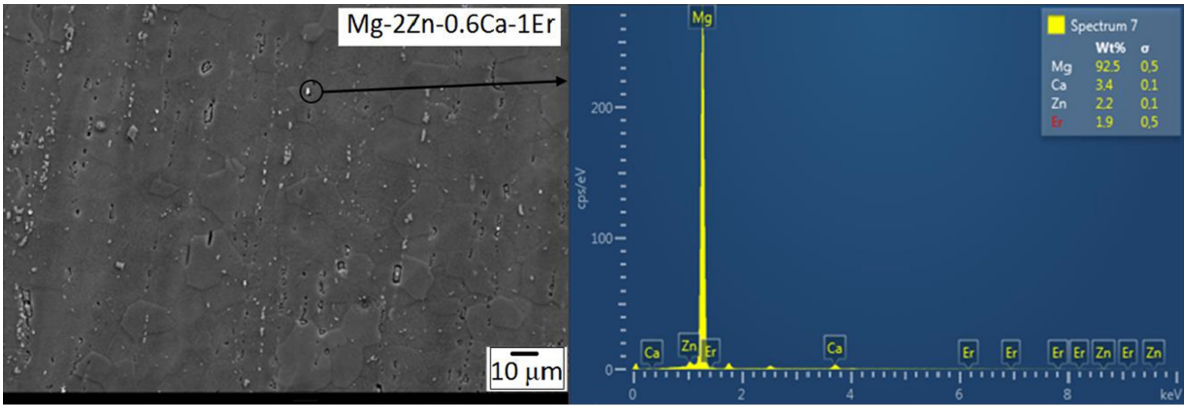

Figure 4. SEM image and EDS-analysis of as-extruded Mg-2Zn-0.6Ca-1Er.

3.1.4. EBSD Studies

To analyze texture and microstructural characteristics, EBSD measurements were carried out. Figure 5 shows the inverse pole figures and pole figures of Mg-2Zn-0.6Ca-1Er extruded at 350 °C with the observation direction parallel to the longitudinal (extruded) direction by using SEM-EBSD. The basal plane texture is strong for pure magnesium but these poles are spread toward a transverse direction (TD) for the alloy. Also, as seen in the pole figures, the basal plane intensity is 7.22 whereas pure Mg showed a higher MUD (Multiples of Uniform density) value of 11.15. This is also seen for Mg-Zn-Ce (Ca) alloy sheets where Zn concentration greater than 0.5 wt.% modified the basal plane texture [27]. TD spread of basal texture has a relationship with the activity of prismatic slip [28]. With the addition of Zn, the basal plane intensity decreased and (100) prismatic texture evolved. Therefore, for Mg-2Zn-0.6Ca-1Er, the overall texture is weakened.

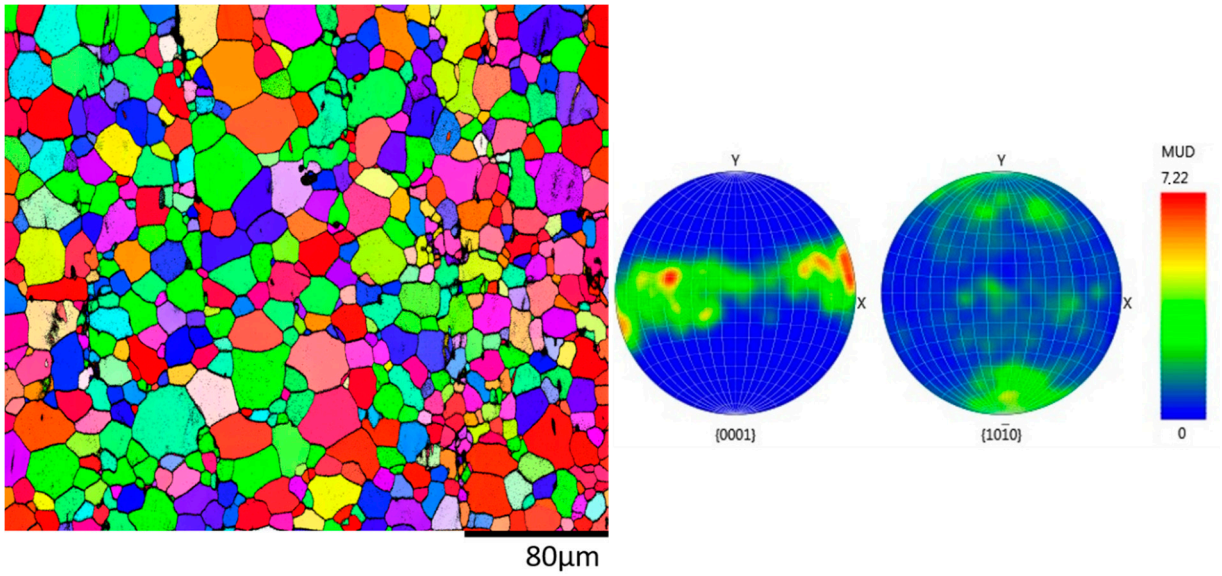

Figure 5. Inverse pole figures and corresponding pole figures for Mg-2Zn-0.6Ca-1Er (where x = Transverse Direction and y = Extrusion Direction).

3.2. Mechanical Properties

3.2.1. Microhardness

The hardness values from the microhardness measurements as seen in Table 1 show an increase in the microhardness value for Mg-2Zn-0.6Ca-1Er as compared to pure Mg. The increment for the alloy is up to 62%. Looking at such an enhancement, it can be safely attributed to the addition of ternary and quaternary alloying elements influenced the hardness value largely. Also, the presence of uniformly distributed and harder secondary phases formed during DMD and hot-extrusion could be the reason, along with reduced grain sizes that can act as a constraint to a local deformation produced during the indentation procedure.

Table 1. Vickers microhardness values and grain size of Mg and its alloys.

Material/Alloy	Hardness (Hv)	Grain Size (µm)	% Hardness Increment
Pure Mg	33.84	22.42	-
Mg-2Zn-0.6Ca-1Er	55.04	11.57	62.64

3.2.2. Tensile Properties

The tensile test results of Mg-2Zn-0.6Ca-1Er is shown in Figure 6, along with the curves of pure Mg for reference. These are representative curves out of 5 tests carried out

for each material. From the results, it can be observed that the 0.2% tensile yield strength (0.2% TYS) and tensile fracture strain values have increased significantly with the addition of alloying elements with a reasonable improvement in the ultimate tensile strength (UTS). Pure Mg exhibited TYS and UTS values of 96 ± 3 and 150 ± 3 MPa, respectively. The addition of alloying elements increased the values to 128 ± 4 and 225 ± 2 MPa, respectively. The ductility values also increased significantly from 8.3 ± 0.2 to 17.2 ± 0.3. The strength and ductility values are tabulated in Table 2.

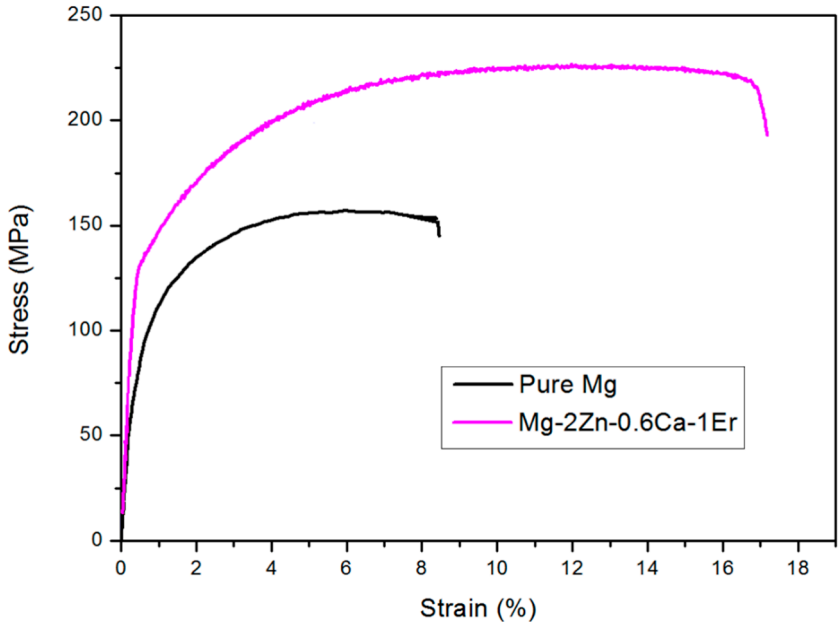

Figure 6. Representative tensile curves of pure Mg and Mg-2Zn-0.6Ca-1Er.

Table 2. Tensile properties of pure Mg and Mg-2Zn-0.6Ca-1Er.

Sl. No	Material	TYS (MPa)	UTS (MPa)	Elongation
1	Pure Mg	96 ± 3	150 ± 3	8.3 ± 0.2
2	Mg-2Zn-0.6Ca-1Er	128 ± 4 (↑33.33%)	225 ± 2 (↑50%)	17.2 ± 0.3 (↑107.2%)

3.2.3. Fractography

Figure 7 shows the tensile fracture surface of Mg-2Zn-0.6Ca-1Er. In the case of pure Mg, fracture occurs by cleavage mode with few ductile features [29]. For the quaternary alloy seen in Figure 7, the fracture behavior is ductile due to several dimples like features that are observed in SEM. These SEM fractography images are in coherence with the ductility values presented in Table 2 for Mg-2Zn-0.6Ca-1Er. Figure 8 shows the microstructures of the as-extruded Mg-2Zn-0.6Ca-1Er alloys after the tensile test. Many twins that could be seen in these alloys contribute to the enhanced ductility values that are shown in Table 2. Hence, it can be said that the alloying elements had a great influence on the fracture behavior of the samples.

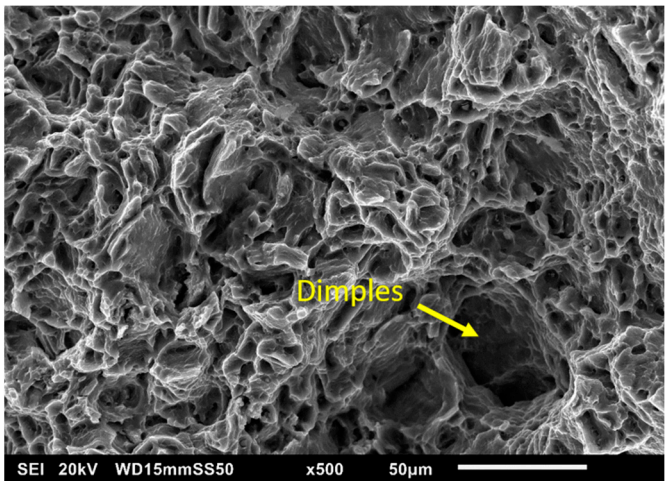

Figure 7. Fractography of as-extruded Mg-2Zn-0.6Ca-1Er.

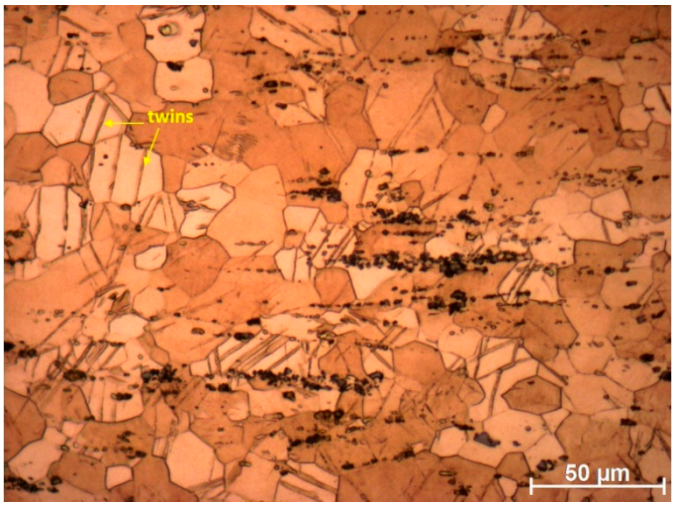

Figure 8. Optical microstructure close to the tensile fractured regions of Mg-2Zn-0.6Ca-1Er.

3.2.4. Damping Properties

The impulse excitation measurement results are tabulated in Table 3. It could be seen that the damping characteristics did not significantly change with the addition of alloying elements. These parameters listed were calculated after plotting the amplitude of vibration versus time and the vibration ceased for the alloys after 0.5 s. The elastic modulus calculated for pure Mg is 45.26 GPa and for the quaternary alloy, the calculated value is 44.45 GPa. It can be noted that the elastic modulus did not change significantly with the addition of Zn, Ca, and Er, which is very important for the biomedical applications of magnesium.

Table 3. Elastic modulus and damping characteristics of pure Mg and Mg-2Zn-0.6Ca-1Er.

Material	Damping Loss Rate	Damping Capacity	Elastic Modulus (GPa)
Pure Mg	7.2	0.000275	45.26
Mg-2Zn-0.6Ca-1Er	6.8	0.000261	44.45

3.3. Corrosion Behavior

3.3.1. Immersion Test

The results of the immersion test in 0.5 wt.% NaCl solution to study the general corrosion behavior of as-extruded alloys at room temperature are plotted in Figure 9. The

inset figure shows a clearer picture of the weight loss measurements for Mg-2Zn-0.6Ca-1Er. Both pure Mg and the quaternary alloy suffered weight loss as a result of corrosion. Pure Mg underwent rapid degradation after the first day of immersion (38% weight loss) and thereafter the degradation process was moderate. A 47% weight loss was recorded for pure Mg after 7 days of immersion in NaCl solution. The edges of the pure Mg sample lost their structural integrity completely, which can be seen in Figure 9. The macrograph for pure Mg after Day 7 of immersion shows that material loss took place mostly at the edges and in the figure with severely corroded regions. However, for Mg-2Zn-0.6Ca-1Er alloy, the degradation process was moderate from 1st day of immersion and there was no rapid degradation as compared to pure Mg. The macrostructure of Mg-2Zn-0.6Ca-1Er shows very little information concerning corrosion. The corrosion rates were calculated and they are tabulated in Table 4. It could be seen that in NaCl medium, pure Mg exhibited corrosion rate of 82.59 mm/y whereas the quaternary alloy exhibited the corrosion rate of 7.83 mm/y. Mg-2Zn-0.6Ca-1Er exhibited the corrosion rate of 1.55 mm/y in PBS solution at 37 °C as compared to 20.91 mm/y exhibited by pure Mg. Hence, it could be seen that the quaternary alloy exhibited greater corrosion resistance in both corrosive environments. However, the results for immersion tests in 0.5 wt.% NaCl medium at human body temperature (37 °C) also could be interesting and they are planned to be conducted.

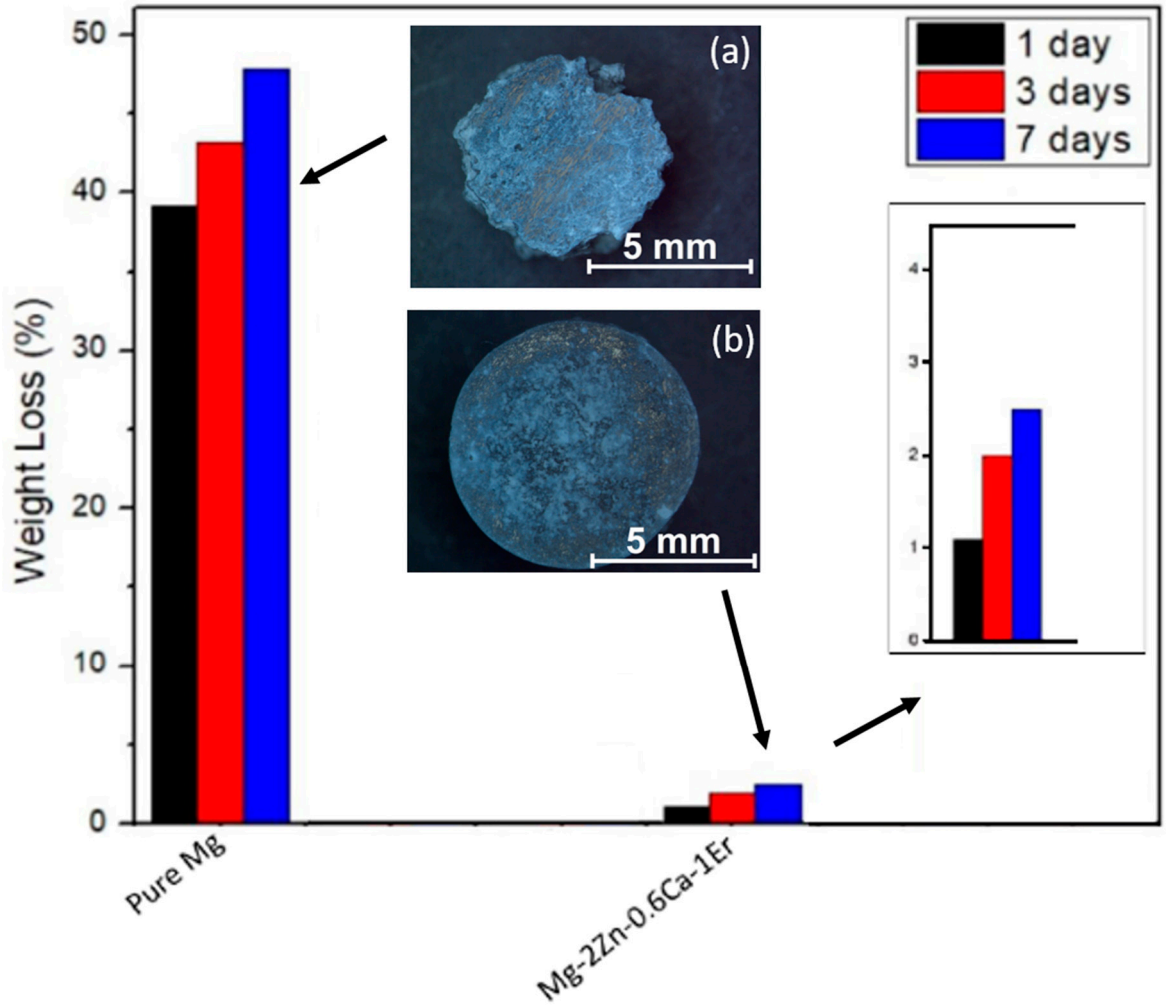

Figure 9. Immersion test results of pure Mg and Mg-2Zn-0.6Ca-1Er in 0.5 wt.% NaCl solution at 37 °C for 1, 3, and 7 days. The graph in the inset is the magnified version of weight loss measurements of Mg-2Zn-0.6Ca-1Er and the macrostructures of (**a**) pure Mg (**b**) Mg-2Zn-0.6Ca-1Er after immersion for 7 days in 0.5 wt.% NaCl solution.

Table 4. Results of hydrogen evolution test and immersion tests performed on pure Mg and the quaternary alloy in NaCl at 25 °C and PBS at 37 °C respectively.

Material	H_2 Evolution Test				Immersion Test					
	NaCl at 25 °C		PBS at 37 °C		NaCl at 25 °C			PBS at 37 °C		
	V_H (mL)	CR (mm/y)	V_H (mL)	CR (mm/y)	Weight Loss (g)	ΔW (mg cm^{-2} d^{-1})	CR (mm/y)	Weight Loss (g)	ΔW (mg cm^{-2} d^{-1})	CR (mm/y)
Pure Mg	19.2	43.76	8.75	19.94	0.1762	39.33	82.59	0.0446	9.955	20.91
Mg-2Zn-0.6Ca-1Er	4.32	9.85	1.75	3.99	0.0167	3.728	7.83	0.0033	0.7366	1.55

3.3.2. Hydrogen Evolution Test

The results of H_2 evolution test in 0.5 wt.% NaCl and PBS solution for as-extruded pure Mg and Mg-2Zn-0.6Ca-1Er are tabulated in Table 4. For pure Mg, the degradation in NaCl medium was rapid and volume of hydrogen (mL cm^{-2} d^{-1}) evolved was found to be 19.2 mL. The quaternary alloy evolved lower hydrogen values and it was found to be 4.32 mL per day. Using the formula, the corrosion rate (mm/y) was calculated to be 43.76 and 9.85 respectively. Tests conducted in PBS solution at 37 °C showed a slight decrease in the volume of hydrogen evolved. For pure Mg, the volume of hydrogen (mL cm^{-2} d^{-1}) was found to be 8.75 mL. The quaternary alloy evolved lower hydrogen values and it was found to be 1.75 mL per day. Using the formula, the corrosion rate (mm/y) was calculated to be 19.94 and 3.99, respectively.

4. Discussion

In tailoring the microstructure, several aspects like grain size, distribution of secondary phases, and effect of extrusion on improving the mechanical and corrosion behavior are discussed as follows.

4.1. Grain Size

The grain size of the as-DMDed alloy can be varied by changing the composition of the alloy for a defined set of conditions. Also, the grain sizes could be controlled by several means like an undercooling parameter, solidification interval, etc.

The addition of alloying elements subsequently reduced the grain size. With reduction in the grain size, the movement of dislocation will be prevented due to an increased fraction of boundaries. Trace addition of Er to reduce the grain sizes of Mg-Zn-Zr alloy was done by Zhang et al. [30]. The Er addition on Mg-Al alloys was studied by Seetharaman et al. [21]. The reduction in grain size was attributed to the capability of Al-Er related phases for grain nucleation and grain growth restriction. These elements are capable of segregating at the front of grain growth. Restriction of grain growth takes place due to an intensive constitutional undercooling in a diffusion layer ahead of the advancing solid/liquid interface [31]. Also, Er solute atoms exert a drag force on the grain boundary motion.

4.2. Extrusion and Mechanical Properties

The increase in the mechanical properties after thermomechanical processing like hot-extrusion is due to the complicated ramification of the coarse-grained as-DMDed microstructure of the starting ingot. During extrusion, several combinations of processes like deformation, recrystallization, and grain growth take place. Also, the dispersion, dissolution, and formation of certain new phases may take place during this process [21]. The coarse phases that were present in as-DMDed alloys were broken during hot-extrusion. These second phase particles can either retard or accelerate recrystallization kinetics, depending on its size. These particles have a significant effect during plastic deformation on the texture and mechanical properties of alloys. When the size of the second phase particles is greater than 1μm, they can be possible nucleation sites for recrystallization. This leads to the formation of new grains by accommodating the increased misorientation

of the cells of the substructure. This phenomenon is called particle-stimulated nucleation (PSN) [32]. A refined grain structure is obtained for the alloys, with refined grains in the vicinity of these hard secondary phases. These particles are ideal nucleation sites for recrystallization and exert a pinning effect on the grain boundaries to prevent the growth of dynamic recrystallized (DRXed) grains. The particles leading to DRX via PSN could also be seen for several different Mg-based alloys [33].

An increase in dislocation density during plastic deformation affects strain hardening behavior. This results in a dislocation tangle that leads to the obstruction of the dislocation movement [34]. For the plastic deformation of a material, the stress required is directly proportional to the dislocation density. Factors including grain size, presence of solute atoms, grain orientation, and secondary phases affect the dislocation behavior and strain hardening behavior.

Grain Size, Solid Solution Strengthening, and Particle Strengthening

The smaller the grains, the more is the applied stress to move a dislocation across the grain boundary and hence higher the yield strength. This phenomenon is known as the Hall-Petch effect and the increase in the yield strength value for the alloys is attributed to this effect. Also, due to the enhanced solubility of the alloying elements like calcium, zinc, and erbium in magnesium, these alloying elements lead to solution hardening by remaining as dispersed solutes and impede the movement of dislocations. The elements are introduced within their solubility limit and the interruption in the regularity of Mg crystal lattice requires activation in the form of temperature or stress for the movement of dislocations.

These secondary phases with a high hardness aligned along the extrusion direction can accumulate stress near the particle-matrix interface due to de-cohesion. Hence, the deformation of the matrix can be blocked by these fine particles during the tensile and compressive tests. The same phenomenon has been reported by Wang et al. on Mg-Zn-Er alloys [35]. The secondary phases that are distributed uniformly can provide sufficient dispersion strengthening to the alloys by pinning the dislocations. Among all the alloys, Mg-2Zn-0.6Ca-1Er shows the highest ductility of 17.2%. The improvement in ductility is attributed to weaker texture due to Er addition. A similar behavior was observed by Yang et al. [36] for reduced graphene oxide reinforced Zn scaffold composite synthesized by laser additive manufacturing where the reinforcement weakened the texture and enhanced both strength and ductility.

4.3. Corrosion Behavior

4.3.1. Grain Size and Secondary Phases

Grain size refinement of pure Mg without alloying additions has enhanced the corrosion resistance [37]. The grain size of α-phase also plays a major role. This is an important microstructural parameter other than the presence of secondary phases. If there is complete recrystallization taking place after hot-extrusion, the specimens with equiaxed grain structure can exhibit better corrosion resistance over as-cast samples [38]. The intensity of micro galvanic coupling reduces due to an increased fraction of grain boundaries with a reduction in grain size [39]. A decrease in the weight loss and H_2 evolution as seen in Table 4 for the quaternary alloy was influenced significantly by the presence and distribution of secondary phases, which are more cathodic and are thermodynamically stable than Mg. Since these phases are cathodic to the matrix, the galvanic effect would likely persist. Corrosion in Mg-Al alloys with a coarse grain structure takes place due to the presence of discontinuously distributed β phase. Conversely, in a grain refined microstructure of Mg-2Zn-0.6Ca-1Er, the secondary phases are distributed finely and continuously that can inhibit the development of corrosion. A similar result was obtained by Yang et al. for laser additive manufactured ZK60 alloy, where a reduced corrosion rate was observed for fine grained microstructure [40].

To simulate the corrosion phenomenon, a schematic diagram is represented in Figure 10 for Mg-2Zn-0.6Ca-1Er. The second phase particles which are cathodic to the matrix lead to micro-galvanic coupling due to the difference in their standard electrochemical potentials. However, these second phase particles which are small and continuously distributed both inside and along the grain boundaries stop corrosion from grain to grain, as represented in the figure, termed as barrier effect. Therefore, the corrosion rate of Mg-2Zn-0.6Ca-1Er is lower.

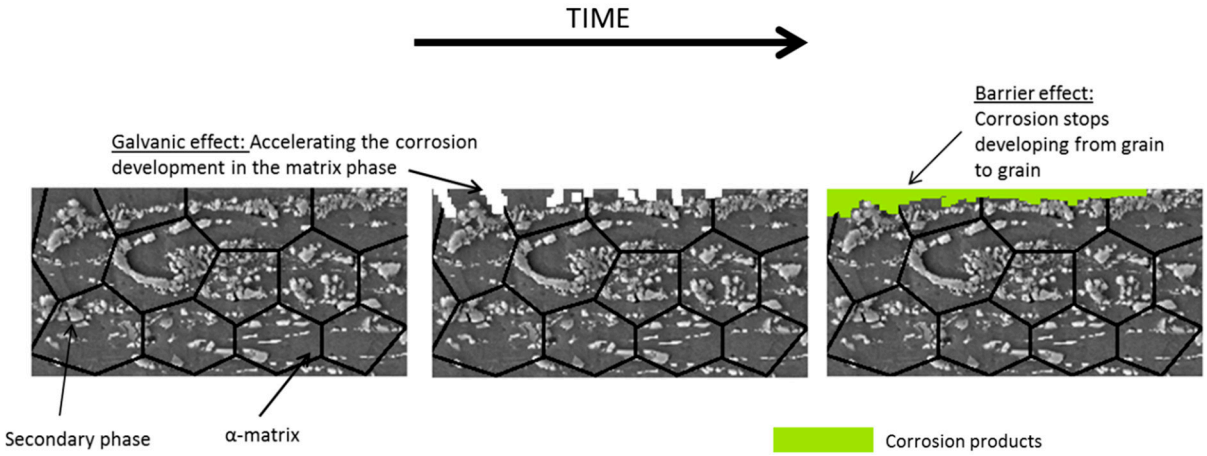

Figure 10. Schematic diagrams of morphology during the corrosion process.

4.3.2. Effect of Alloying Elements

Addition of zinc to magnesium reduces the corrosion rate due to the increase in its charge transfer resistance [41]. Zhang et al. [41] studied corrosion behavior of Mg-6Zn alloy and it displayed excellent in-vitro biocompatibility characteristics. Alloying Zn to Mg has improved its corrosion characteristics, as observed by Kubasek et al. [42]. However, increased Zn concentration can lead to the enhanced Mg_xZn_y secondary phases that could contribute to micro-cathodic effect and enhance the corrosion rate. Therefore, 2 wt.% Zn was added in the alloy to optimize both increase in mechanical properties and corrosion resistance.

The low-density value of Ca like Mg endues this Mg-Ca system to be studied as bio-implants due to the advantage of similar density to that of bone. Since Ca is a major component in human bone and essential in chemical signaling with cells, the release of Ca^{2+} and Mg^{2+} ions during biodegradation is expected to be beneficial to bone healing. The degradation rate of our alloy with 0.6Ca addition has reduced. The redox potential of Ca is more negative ($-2.76V_{SCE}$) than that of pure Mg ($-2.37V_{SCE}$) and hence the Ca part becomes anodic. However, since a very minimal addition is introduced (0.6 wt.%), it acts as a grain refiner and thus leads to a reduction in the corrosion rate.

Rare-earth addition like erbium is known to be beneficial in slowing down the corrosion kinetics of Mg alloys [21]. The distribution and composition of secondary phases due to the addition of Er plays a very important role in modifying the electrochemical behavior of the alloys.

4.4. Biocompatibility and Biomechanical Properties of the Alloys

Two of the important mechanical properties to investigate for metallic implants targeting orthopedic applications are elastic modulus and damping capacity. The stimulation of new bone growth is decreased due to the stress-shielding effect caused by high elastic moduli implants such as steel and titanium, and it leads to implant failure. High damping capacity implants made of magnesium helps in mitigating the vibrations caused when the patient moves and it helps in suppressing the stresses developed at the bone/implant interface. Apart from them, an excellent combination of strength and ductility to prolong

the degradation and avoid mechanical failure is required as the patient is always subjected to both static and repetitive loads. These levels must be high enough to compensate for the degradation of the implant as the new bone forms. With the low amount of alloying additions, the tensile properties have been enhanced, as seen in Table 2, and these materials can provide sufficient support as an orthopedic implant [43]. The elements zinc, calcium, and erbium are biocompatible only when their additions are within the toxicity levels. The weight loss measurements as seen in Figure 9 are low for Mg-2Zn-0.6Ca-1Er as compared to pure Mg. Since low alloying additions have been introduced, the synthesized Mg-2Zn-0.6Ca-1Er alloy could be a viable candidate for potential orthopedic implants in the future.

5. Conclusions

The combined effects of zinc, calcium and erbium addition were investigated on the microstructure, mechanical, and corrosion behavior of as-extruded Mg alloys. The processing methodology ensured dense and defect-free products. The influence of alloying elements contributed to enhanced mechanical properties. The TYS, UTS and ductility values of the quaternary alloy are 128 MPa, 225 MPa, and 17.2%, respectively, and it can be attributed to the reduction in grain size (11.57 µm), solid-solution strengthening, and the uniformly distributed fine secondary phases. The immersion test experiments to study the general corrosion behavior using 0.5 wt.% NaCl at 25 °C exhibited a corrosion rate of 82.59 mm/y for pure Mg after 7 days. However, Mg-2Zn-0.6Ca-1Er alloy did not lose its structural integrity and exhibited the corrosion rate of 7.83 mm/y. The reduced corrosion behavior is attributed to the barrier effect caused by the secondary phases that has modified the electrochemical behavior of the quaternary alloy.

Author Contributions: Conceptualization, D.B.P. and R.S.; Methodology, D.B.P., R.S. and M.G.; Data Curation, D.B.P.; Writing–Original Draft Preparation, D.B.P.; Writing–Review & Editing, D.B.P. and R.S.; Supervision, R.S. All authors have read and agreed to the published version of the manuscript.

Funding: This research received no external funding.

Institutional Review Board Statement: Not applicable.

Informed Consent Statement: Not applicable.

Data Availability Statement: Not applicable.

Acknowledgments: One of the authors, Devadas Bhat Panemangalore (D.B.P.) sincerely thanks University Lille doctoral research grant for supporting his graduate program. The SEM national facility in Lille (France) is supported by the Conseil Regional du Hauts-de-France and the European Regional Development Fund (ERDF).

Conflicts of Interest: The authors declare no conflict of interest.

References

1. Witte, F.; Hort, N.; Vogt, C.; Cohen, S.; Kainer, K.U.; Willumeit, R.; Feyerabend, F. *Degradable Biomaterials Based on Magnesium Corrosion*; Elsevier: Amsterdam, The Netherlands, 2008; Volume 12, ISBN 4951153548.
2. Song, G.; Atrens, A.; Stjohn, D.; Nairn, J.; Li, Y. The electrochemical corrosion of pure magnesium in 1 N NaCl. *Corros. Sci.* **1997**, *39*, 855–875. [CrossRef]
3. Yan, T.; Tan, L.; Xiong, D.; Liu, X.; Zhang, B.; Yang, K. Fluoride treatment and in vitro corrosion behavior of an AZ31B magnesium alloy. *Mater. Sci. Eng. C* **2010**, *30*, 740–748. [CrossRef]
4. Rettig, R.; Virtanen, S. Composition of corrosion layers on a magnesium rare-earth alloy in simulated body fluids. *J. Biomed. Mater. Res. Part A* **2009**, *88*, 359–369. [CrossRef]
5. Yuen, C.K.; Ip, W.Y. Theoretical risk assessment of magnesium alloys as degradable biomedical implants. *Acta Biomater.* **2010**, *6*, 1808–1812. [CrossRef]
6. Li, J.; Du, W.; Li, S.; Wang, Z. Effect of aging on microstructure of Mg-Zn-Er alloys. *J. Rare Earths* **2009**, *27*, 1042–1045. [CrossRef]
7. Zhang, J.; Xu, C.; Jing, Y.; Lv, S.; Liu, S.; Fang, D.; Zhuang, J.; Zhang, M.; Wu, R. New horizon for high performance Mg-based biomaterial with uniform degradation behavior: Formation of stacking faults. *Sci. Rep.* **2015**, *5*, 13933. [CrossRef] [PubMed]
8. Boehlert, C.J.; Knittel, K. The microstructure, tensile properties, and creep behavior of Mg–Zn alloys containing 0–4.4wt.% Zn. *Mater. Sci. Eng. A* **2006**, *417*, 315–321. [CrossRef]

9. Peng, Q.; Li, X.; Ma, N.; Liu, R.; Zhang, H. Effects of backward extrusion on mechanical and degradation properties of Mg-Zn biomaterial. *J. Mech. Behav. Biomed. Mater.* **2012**, *10*, 128–137. [CrossRef] [PubMed]
10. Bakhsheshi-Rad, H.R.; Hamzah, E.; Fereidouni-Lotfabadi, A.; Daroonparvar, M.; Yajid, M.A.M.; Mezbahul-Islam, M.; Kasiri-Asgarani, M.; Medraj, M. Microstructure and bio-corrosion behavior of Mg-Zn and Mg-Zn-Ca alloys for biomedical applications. *Mater. Corros.* **2014**, *65*, 1178–1187. [CrossRef]
11. Parande, G.; Manakari, V.; Kopparthy, S.D.S.; Gupta, M. Utilizing Low-Cost Eggshell Particles to Enhance the Mechanical Response of Mg-2.5Zn Magnesium Alloy Matrix. *Adv. Eng. Mater.* **2017**, 1700919. [CrossRef]
12. Drynda, A.; Hassel, T.; Hoehn, R.; Perz, A.; Bach, F.-W.; Peuster, M. Development and biocompatibility of a novel corrodible fluoride-coated magnesium-calcium alloy with improved degradation kinetics and adequate mechanical properties for cardiovascular applications. *J. Biomed. Mater. Res. Part A* **2010**, *93*, 763–775. [CrossRef]
13. Kannan, M.B.; Raman, R.K.S. In vitro degradation and mechanical integrity of calcium-containing magnesium alloys in modified-simulated body fluid. *Biomaterials* **2008**, *29*, 2306–2314. [CrossRef] [PubMed]
14. Mordike, B.L.; Lukac, P. Physical Metallurgy. In *Magnesium Technology—Metallurgy, Design Data, Applications*; Springer: Berlin/Heidelberg, Germany, 2006.
15. Erdmann, N.; Angrisani, N.; Reifenrath, J.; Lucas, A.; Thorey, F.; Bormann, D.; Meyer-Lindenberg, A. Biomechanical testing and degradation analysis of MgCa0.8 alloy screws: A comparative in vivo study in rabbits. *Acta Biomater.* **2011**, *7*, 1421–1428. [CrossRef] [PubMed]
16. You, B.-S.; Park, W.-W.; Chung, I.-S. The Effect of Calcium Addition to Magnesium on the Microstructure and Compositional Changes of Oxide Film Formed at High Temperature. *Mater. Trans.* **2001**, *42*, 1139–1141. [CrossRef]
17. Nie, J.F.; Muddle, B.C. Precipitation hardening of Mg-Ca(-Zn) alloys. *Scr. Mater.* **1997**, *37*, 1475–1481. [CrossRef]
18. Li, Z.; Gu, X.; Lou, S.; Zheng, Y. The development of binary Mg-Ca alloys for use as biodegradable materials within bone. *Biomaterials* **2008**, *29*, 1329–1344. [CrossRef]
19. Rim, K.T.; Koo, K.H.; Park, J.S. Toxicological evaluations of rare earths and their health impacts to workers: A literature review. *Saf. Health Work* **2013**, *4*, 12–26. [CrossRef]
20. Leng, Z.; Zhang, J.; Yin, T.; Zhang, L.; Guo, X.; Peng, Q.; Zhang, M.; Wu, R. Influence of biocorrosion on microstructure and mechanical properties of deformed Mg-Y-Er-Zn biomaterial containing 18R-LPSO phase. *J. Mech. Behav. Biomed. Mater.* **2013**, *28*, 332–339. [CrossRef] [PubMed]
21. Seetharaman, S.; Blawert, C.; Ng, B.M.; Wong, W.L.E.; Goh, C.S.; Hort, N.; Gupta, M. Effect of erbium modification on the microstructure, mechanical and corrosion characteristics of binary Mg-Al alloys. *J. Alloys Compd.* **2015**, *648*, 759–770. [CrossRef]
22. Du, X.; Wei, C.; Wu, B.; Hong, M.; Xia, Y.; Li, W. A high-performance Mg-Er-Zn-Zr alloy with low Er/Zn mass ratio. *J. Cent. South Univ.* **2015**, *22*, 4123–4127. [CrossRef]
23. Li, H.; Du, W.; Li, S.; Wang, Z. Effect of Zn/Er weight ratio on phase formation and mechanical properties of as-cast Mg-Zn-Er alloys. *Mater. Des.* **2012**, *35*, 259–265. [CrossRef]
24. Zhao, X.; Li, S.; Wang, Q.; Du, W.; Liu, K. Effects of heat treatment on microstructure and mechanical properties of Mg-5Zn-0.63Er alloy. *Trans. Nonferrous Met. Soc. China* **2013**, *23*, 59–65. [CrossRef]
25. Gupta, M.; Wong, W.L.E. Magnesium-based nanocomposites: Lightweight materials of the future. *Mater. Charact.* **2015**, *105*, 30–46. [CrossRef]
26. Panemangalore, D.B.; Shabadi, R.; Gupta, M.; Ji, G. Effect of fluoride coatings on the corrosion behavior of Mg-Zn-Er alloys. *Surf. Interfaces* **2019**, *14*, 72–81. [CrossRef]
27. Chino, Y.; Huang, X.; Suzuki, K.; Sassa, K.; Mabuchi, M. Influence of Zn concentration on stretch formability at room temperature of Mg-Zn-Ce alloy. *Mater. Sci. Eng. A* **2010**, *528*, 566–572. [CrossRef]
28. Styczynski, A.; Hartig, C.; Bohlen, J.; Letzig, D. Cold rolling textures in AZ31 wrought magnesium alloy. *Scr. Mater.* **2004**, *50*, 943–947. [CrossRef]
29. Meenashisundaram, G.K.; Gupta, M. Synthesis and characterization of high performance low volume fraction TiC reinforced Mg nanocomposites targeting biocompatible/structural applications. *Mater. Sci. Eng. A* **2015**, *627*, 306–315. [CrossRef]
30. Zhang, J.; Ma, Q.; Pan, F. Effects of trace Er addition on the microstructure and mechanical properties of Mg-Zn-Zr alloy. *Mater. Des.* **2010**, *31*, 4043–4049. [CrossRef]
31. Zhang, E.; Yin, D.; Xu, L.; Yang, L.; Yang, K. Microstructure, mechanical and corrosion properties and biocompatibility of Mg-Zn-Mn alloys for biomedical application. *Mater. Sci. Eng. C* **2009**, *29*, 987–993. [CrossRef]
32. Humphreys, J.; Rohrer, G.S.; Rollett, A.; Humphreys, J.; Rohrer, G.S.; Rollett, A. Chapter 9—Recrystallization of Two-Phase Alloys. In *Recrystallization and Related Annealing Phenomena*; Elsevier: Amsterdam, The Netherlands, 2017; pp. 321–359. ISBN 9780080982359.
33. Robson, J.D.; Henry, D.T.; Davis, B. Particle effects on recrystallization in magnesium—Manganese alloys: Particle-stimulated nucleation. *Acta Mater.* **2009**, *57*, 2739–2747. [CrossRef]
34. Chen, X.; Pan, F.; Mao, J.; Wang, J.; Zhang, D.; Tang, A.; Peng, J. Effect of heat treatment on strain hardening of ZK60 Mg alloy. *Mater. Des.* **2011**, *32*, 1526–1530. [CrossRef]
35. Wang, Q.; Du, W.; Liu, K.; Wang, Z.; Li, S.; Wen, K. Microstructure, texture and mechanical properties of as-extruded Mg-Zn-Er alloys. *Mater. Sci. Eng. A* **2013**, *581*, 31–38. [CrossRef]

36. Yang, Y.; Cheng, Y.; Peng, S.; Xu, L.; He, C.; Qi, F.; Zhao, M.; Shuai, C. Microstructure evolution and texture tailoring of reduced graphene oxide reinforced Zn scaffold. *Bioact. Mater.* **2021**, *6*, 1230–1241. [CrossRef] [PubMed]
37. Birbilis, N.; Ralston, K.D.; Virtanen, S.; Fraser, H.L.; Davies, C.H.J. Grain character influences on corrosion of ECAPed pure magnesium. *Corros. Eng. Sci. Technol.* **2010**, *45*, 224–230. [CrossRef]
38. Jeong, Y.S.; Kim, W.J. Enhancement of mechanical properties and corrosion resistance of Mg-Ca alloys through microstructural refinement by indirect extrusion. *Corros. Sci.* **2014**, *82*, 392–403. [CrossRef]
39. Argade, G.R.; Panigrahi, S.K.; Mishra, R.S. Effects of grain size on the corrosion resistance of wrought magnesium alloys containing neodymium. *Corros. Sci.* **2012**, *58*, 145–151. [CrossRef]
40. Yang, Y.; He, C.; Dianyu, E.; Yang, W.; Qi, F.; Xie, D.; Shen, L.; Peng, S.; Shuai, C. Mg bone implant: Features, developments and perspectives. *Mater. Des.* **2020**, *185*, 108259. [CrossRef]
41. Zhang, S.; Li, J.; Song, Y.; Zhao, C.; Zhang, X.; Xie, C.; Zhang, Y.; Tao, H.; He, Y.; Jiang, Y.; et al. In vitro degradation, hemolysis and MC3T3-E1 cell adhesion of biodegradable Mg-Zn alloy. *Mater. Sci. Eng. C* **2009**, *29*, 1907–1912. [CrossRef]
42. Kubásek, J.; Vojtěch, D. Structural characteristics and corrosion behavior of biodegradable Mg-Zn, Mg-Zn-Gd alloys. *J. Mater. Sci. Mater. Med.* **2013**, *24*, 1615–1626. [CrossRef] [PubMed]
43. Tekumalla, S.; Seetharaman, S.; Almajid, A.; Gupta, M. Mechanical Properties of Magnesium-Rare Earth Alloy Systems: A Review. *Metals* **2014**, *5*, 1. [CrossRef]